ELSEVIER

Contents lists available at ScienceDirect

Chemical Engineering Journal

journal homepage: www.elsevier.com/locate/cej



Hollow raspberry-like nanoaggregates for sensitive SERS detection of PAHs in water

Huimin Xie ^{a,1}, Shuyu Zhu ^{a,b,1}, Jingwen Cao ^a, JuHyeong Lee ^c, Yidan Yin ^d, Deyue Zhou ^d, Jing Yan ^e, Hyeon-Ho Jeong ^c, Tung-Chun Lee ^{d,*}, Yuewen Zhang ^{a,*}, Qiaosheng Pu ^a, Yang Lan ^{b,*}

- ^a College of Chemistry and Chemical Engineering, Lanzhou University, Lanzhou 730000, China
- ^b Department of Chemical Engineering, University College London, London WC1E 7JE, United Kingdom
- c School of Electrical Engineering and Computer Science, Gwangju Institute of Science and Technology, 61005 Gwangju, Republic of Korea
- d Institute for Materials Discovery, University College London, London WC1H OAJ, United Kingdom
- ^e Department of Veterinary Medicine, University of Cambridge, Cambridge CB3 0ES, United Kingdom

ARTICLE INFO

Keywords:

Polycyclic Aromatic Hydrocarbons (PAHs) Surface-Enhanced Raman Spectroscopy (SERS) Hollow raspberry-like nanoaggregates Gold Nanoparticles (Au NPs) Environmental water detection

ABSTRACT

Polycyclic aromatic hydrocarbons (PAHs) are significant environmental contaminants with considerable health risks, emphasizing the need for effective monitoring and identification. On-site detection of PAHs using surface-enhanced Raman scattering (SERS) remains challenging due to their weak adsorption on substrates and potential interference from the substrates themselves. To address these challenges, we developed hollow raspberry-like plasmonic nanoaggregates made of functionalized-polystyrene hollow microspheres (HM) decorated with gold nanoparticles (Au NPs). These nanoaggregates feature a hydrophobic inner cavity that effectively enriches PAHs, improving detection sensitivity. Through enhanced plasmonic coupling by carefully controlling Au NPs coverage on polystyrene (PS) surfaces, functionalizing the amino groups on the microsphere surface, and fine-tuning the Au NP to PS ratio, our method achieved detection limits of 4×10^{-8} M for pyrene, 6×10^{-7} M for fluorene, and 4×10^{-7} M for benzo[a]anthracene. Moreover, this approach was effectively utilized for detecting PAHs in both Yellow River water and tap water. This study highlights the capabilities of hollow raspberry-like plasmonic nanoaggregates for qualitative and quantitative analysis of PAHs, thereby broadening the use of advanced nanomaterials in monitoring environmental water quality.

1. Introduction

Polycyclic aromatic hydrocarbons (PAHs) are persistent organic pollutants mainly produced by the incomplete burning of fossil fuels and organic substances [1–3]. Human activities contribute significantly to PAHs contamination in both terrestrial and aquatic ecosystems [4], resulting in considerable environmental damage [5]. Long-term exposure to low concentrations of PAHs is associated with severe health problems, including asthma, cardiovascular disease, and dementiarelated disorders [6–8]. Given their carcinogenic nature at low concentrations, there is an urgent need for precise and efficient methods to detect PAHs [9].

Surface-enhanced Raman spectroscopy (SERS) is an effective method for identifying molecular fingerprints. This technique significantly

amplifies signals at the single-molecule level through plasmonic "hotspots", which arise from strong local electromagnetic fields generated at the gaps between nanostructures or certain anisotropic nanostructures [10,11]. Creating these hotspots is essential for attaining single-molecule sensitivity in Raman detection. However, producing these hotspots necessitates a particular nanoparticle configuration, which restricts the broader applicability of SERS [12–15]. Drawing inspiration from raspberry structures, researchers have created raspberry-like materials featuring evenly spaced nanoparticles. The gaps between these particles can produce Raman signal enhancements ranging from 10⁴ to 10^8 , contingent on the distance between the nanoparticles [16–20].

Despite these advancements, Raman spectroscopy is notably sensitive to the highly polarizable C-C and C=C bonds present in PAHs, making it a powerful tool for elucidating their structural and

E-mail address: yang.lan@ucl.ac.uk (Y. Lan).

^{*} Corresponding authors.

¹ These authors contributed equally.

compositional characteristics [21]. However, strong fluorescence is often associated with PAHs that possess extensive π -conjugated ring systems or functional groups that enhance electronic transitions [22], causing fluorescence emission to shift into the spectral region where Stokes shifts are observed [23]. PAHs typically exhibit electronic transitions in the 200-400 nm spectral region [24,25], resulting in weak Raman scattering under non-resonance conditions such as 532 nm, 633 nm, 785 nm, compared to other compounds. Additionally, the aquatic matrix, including water and dissolved substances, can significantly impact SERS performance. Matrix components may interfere with the interaction between PAHs and the SERS substrate, leading to signal attenuation or masking. Furthermore, competition adsorption between PAHs and other molecules can further reduce the observed Raman signals. Another major challenge for SERS detection is the limited affinity of PAHs for nanostructured gold or silver surfaces continues to pose a significant challenge for SERS detection, resulting in high detection limits [9,26]. One approach to address this challenge is to enhance the concentration of PAHs at SERS hotspots [27]. Various methods have been utilized to increase the concentration of analytes on SERS substrates. At molecular level, cage-like molecules featuring hydrophobic cavities, such as cucurbiturils (CBs), β -cyclodextrin (β -CD), and calix [4] arene, have been employed to enhance SERS signal by creating hostguest complexes that capture analytes [28-30]. In addition, multifunctional adsorption materials like graphene and carbon nanotubes can aid the detection of aromatic analytes, such as pyrene and anthracene, by capturing them through π - π electronic interactions [31,32].

Furthermore, hollow structures composed of gold or silver enhance SERS signals by providing increased surface areas for analytes adsorption [33–35]. Similarly, hollow polymer microspheres enhance the adsorption of hydrophobic compounds in aqueous environments due to their inherent hydrophobic cavities [36–39]. For example, Yang *et al.* showed a notable enrichment of organic molecules inside hollow microspheres, reaching an almost 400-fold concentration of 1-phenylethanol in water [40]. Among numerous polymers, polystyrene (PS) microspheres exhibit excellent adsorption of PAHs compared to similar polymers such as polyethylene terephthalate (PET), high-density polyethylene (HDPE), polyvinyl chloride (PVC), low-density polyethylene (LDPE), and polypropylene (PP) [41,42].

In this study, we report hollow raspberry-like nanoaggregates composed of hollow PS microspheres and gold nanoparticles (Au NPs) as SERS substrates for the detection of PAHs. Compared to conventional core–shell structures, hollow hydrophobic PS microcavities offer significant advantages in enhancing the accumulation of PAHs on SERS substrates. The inherent hydrophobicity of these cavities promotes analyte enrichment, while the raspberry-like structure provides a larger specific surface area and additional adsorption sites. This results in a significantly increased local analyte concentration at SERS hotspots, thereby enhancing signal intensity. Furthermore, the electrostatic self-assembly of raspberry nanoaggregates enables precise control over the surface coverage of Au NPs on the hollow PS microspheres. This allows fine-tuning of interparticle spacing, optimizing hotspot formation for improved SERS sensitivity, enhanced detection performance, and greater colloidal stability.

2. Experimental and simulation section

2.1. Materials

Gold chloride trihydrate (HAuCl₄·3H₂O), sodium citrate (> 98 %) and styrene (St > 99 %) were purchased from Aladdin Reagent (Shanghai) Co. Sodium 4-vinylbenzenesulfonate (Svb > 90 %), divinylbenzene (DVB > 80 %), 2,2′-azobis[2-methylpropionamidine] dihydrochloride (AIBA > 99 %), 2-(acetoacetoxy)ethylmethacrylate (AEMA > 95 %), 2-aminoethyl methacrylate hydrochloride (AEMH > 90 %), potassium persulfate ($K_2S_2O_8 > 99.5$ %) were purchased from Shanghai Macklin Biochemical Technology Co., Ltd. Milli-Q water was

used in all experiments. Environmental water for testing included the Yellow River water and tap water. The Yellow River water underwent pre-treatment, where the suspensions were filtered three times using a 0.22 μ m microporous filter. The tap water did not require this step. Both types of water were then spiked with PAHs at different concentrations (1, 5, and 10 μ M).

2.2. Characterization

UV–visible (UV–Vis) spectroscopy was performed using a Tecan spark 10 M enzyme-labeled instrument to characterize the synthesized Au NPs and nanoaggregates. Dynamic light scattering (DLS) and zeta potential (ζ –potential) measurements were performed using a Brookhaven 90Plus Pals instrument. Centrifugation was performed with a CENCE H1650 centrifuge. Transmission electron microscopy (TEM) images were captured with a JEM-2100 at an accelerating voltage of 200 kV. Scanning electron microscopy (SEM) images were obtained with Hitachi S-4800 and JSM-6701F.

2.3. SERS detection

Raman spectroscopy was performed using a Raman spectrometer (Lab RAEMHR, Evolution-HORIBA FRANCE SAS) with a 633 nm helium-neon laser. The SERS substrates of functionalized hollow raspberrylike nanoaggregates were prepared by mixing a solution of Au NPs with functionalized hollow microspheres (h-PS_b⁺) in a 150:1 vol ratio. After observing a color transition from red to purple, a specific concentration of analyte solution (R6G, Pyr, Flu, and BaA) was introduced, resulting in a total solution volume of 300 μ L. The mixture was incubated for 5 min before being transferred to a quartz cuvette with a 2 mm optical path for detection. Each sample underwent three repeat measurements, and the results were averaged for analytical purposes. Laser power was monitored using a THORLABS PM100A laser power meter after each experiment. The resultant signal intensity was expressed as counts s⁻¹ mW⁻¹ after data conversion. Data processing employed the asymmetric least squares (ALS) technique for baseline correction, and a calibration curve was established based on characteristic peak intensities.

2.4. Synthesis of Au NPs

Au NPs of varying sizes were synthesized via a seeded growth strategy [43]. Initially, 150 mL of 2.2 mM sodium citrate was dissolved in deionized water and heated to boiling with magnetic stirring and a reflux condenser in an oil bath. After boiling for 5 min, 1 mL of HAuCl₄ (25 mM) was injected and reacted for about 30 min to form Au seeds. For the synthesis of Au NPs-1 (10 nm), the reaction mixture was cooled to 90 °C after the Au seeds synthesis, followed by injecting 1 mL of HAuCl₄ (25 mM) and reacting for 30 min, a process repeated twice. Au NPs-2 (23 nm) was prepared using Au NPs-1 as the seed solution. In this step, 55 mL of Au NPs-1 was mixed with 53 mL of deionized water and 2 mL of sodium citrate (60 mM). The solution was heated to 90 °C, 1 mL of HAuCl₄ (25 mM) was injected and reacted for 30 min, with this process repeated twice. For the synthesis of Au NPs-3 (33 nm), Au NPs-4 (42 nm), and Au NPs-5 (54 nm), dilution growth steps were repeated using previous-generation Au NPs as the seed solution. All solutions were protected from light and stored at 4 °C.

2.5. Synthesis of seed PS microspheres

Amino-functionalized positively charged PS microspheres (PS $^+$) were synthesized by adding 0.15 mmol of AEMA and 0.75 mmol AIBA to 150 mL of deionized water. This mixture was degassed under nitrogen at room temperature for 60 min before heating to 80 $^{\circ}$ C, and then 75 mmol of St was added via syringe under nitrogen atmosphere. Polymerization proceeded vigorously at 80 $^{\circ}$ C for 24 h. The resulting PS $^+$ microspheres were purified by centrifugation, washed thrice with deionized water,

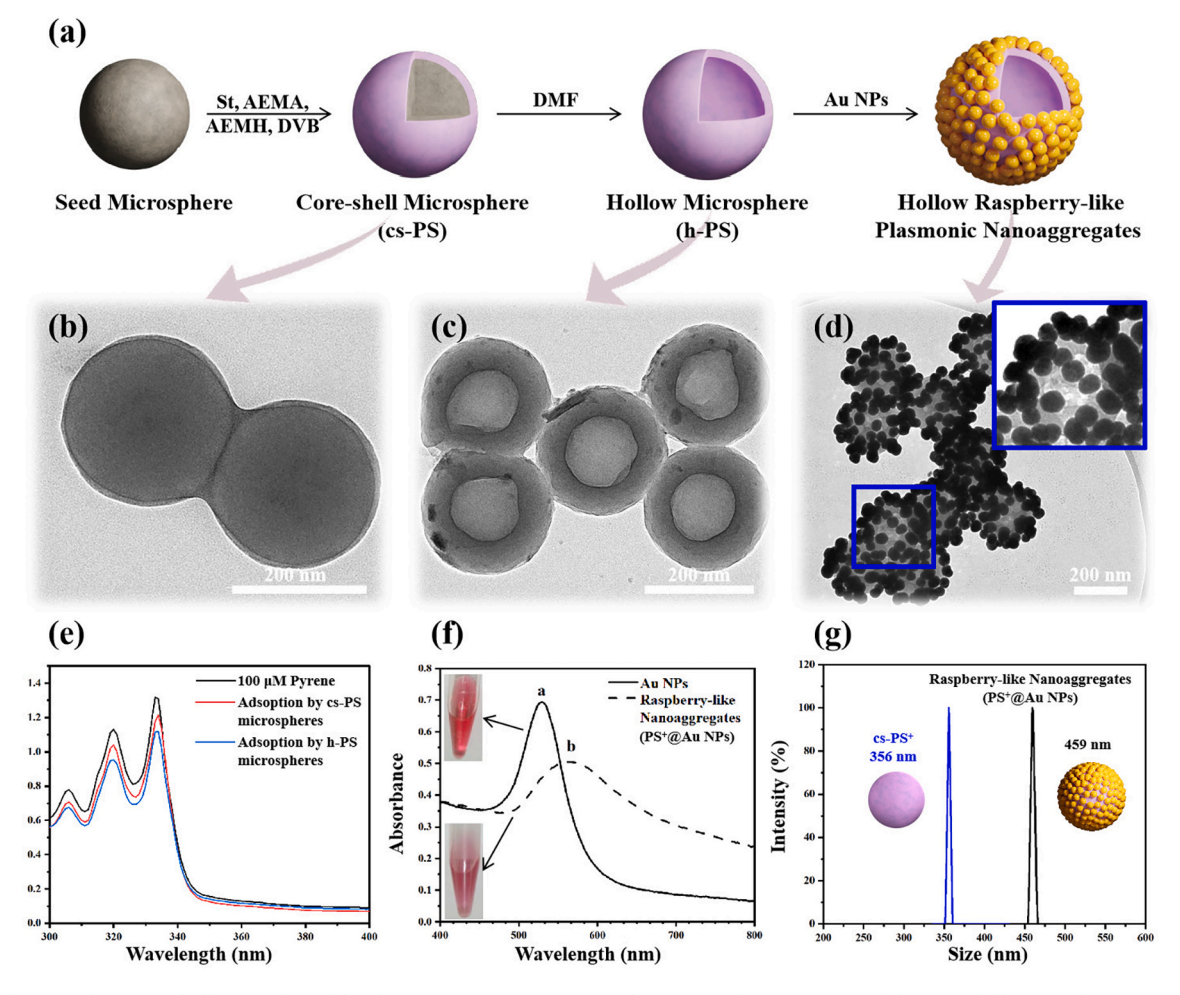


Fig. 1. (a) Schematic diagram of hollow raspberry-like plasmonic nanoaggregates synthesis. TEM characterization of (b) core–shell microspheres (cs-PS); (c) hollow microspheres (h-PS); (d) hollow raspberry-like plasmonic nanoaggregates (scale bar: 200 nm); (e) UV–Vis spectrum of 100 μ M Pyr and the supernatant after adsorption by core–shell polystyrene (cs-PS) and hollow polystyrene (h-PS) microspheres, respectively; (f) UV–Vis spectrum of Au NPs and raspberry-like nanoaggregates (PS $^+$ @Au NPs) and (g) hydrodynamic diameters of PS $^+$ and raspberry-like nanoaggregates (PS $^+$ @Au NPs).

and re-dispersed in 150 mL of deionized water.

To synthesize carbonyl-functionalized negatively charged PS microspheres (PS'), 0.075 mmol Svb and 0.75 mmol $K_2S_2O_8$ were added to 150 mL of deionized water. The mixture underwent nitrogen degassing at room temperature for 60 min, followed by heating to 80 °C. St (75 mmol) was added dropwise using a syringe needle under nitrogen atmosphere, and polymerization proceeded vigorously at 80 °C for 24 h. The resulting PS' microspheres were purified by centrifugation, washed thrice with deionized water, and re-dispersed in 150 mL of deionized water.

2.6. Synthesis of functionalized core-shell microspheres

Functionalized core–shell microspheres were synthesized to control the ratio of carbonyl and amino groups on the microsphere surfaces with specific amount of AEMA and AEMH (Fig. 1a). Initially, an aqueous dispersion of PS $^+$ colloids (45 mL) and 0.5 mmol of AIBA were added to 55 mL of deionized water. After nitrogen degassing for 60 min at room temperature, the mixture was magnetically stirred at 80 °C, with subsequent steps generating core–shell microspheres with crosslinked PS shell. Amino-functionalized core–shell microspheres (cs-PS ^+_a) were synthesized by adding a mixture of 15 mmol St, 0.5 mmol of AEMH, and 1 mmol of DVB. Bifunctionalized core–shell microspheres with an amino to carbonyl ratio of 2:1 (cs-PS ^+_b) was produced by combining 15 mmol of St, 0.5 mmol of AEMH, 0.25 mmol of AEMA, and 1 mmol of DVB. For bifunctionalized core–shell microspheres with a 1:1 amino to carbonyl

ratio of (cs-PS_c^+), a mixture of 15 mmol of St, 0.5 mmol of AEMH, 0.5 mmol of AEMA and 1 mmol of DVB was used. Bifunctionalized coreshell microspheres with a 1:2 amino to carbonyl ratio of (cs-PS_d^+) were synthesized by adding 15 mmol of St, 0.25 mmol of AEMH, 0.5 mmol of AEMA and 1 mmol of DVB. Finally, carbonyl-functionalized core–shell Microspheres (cs-PS_e^+) were obtained by adding 15 mmol of St, 0.5 mmol of AEMA, and 1 mmol of DVB. Each mixture was added dropwise using a syringe over a 10-minutes period.

2.7. Preparation of hollow microspheres

Functionalized core–shell microspheres were dispersed in DMF and placed in a centrifuge tube at room temperature. DMF was replaced every 4 h, repeated four times to ensure complete dissolution of the linear PS core. Following three washes with DMF, the hollow microspheres were rinsed thrice with deionized water and dispersed in deionized water.

2.8. Adsorption performance of core-shell and hollow microspheres for pyrene (Pyr)

Core-shell and hollow microspheres were separately mixed with a 200 μ M Pyr ethanol solution at 1:1 vol ratio. After 3 h of static mixing, the mixture underwent centrifugation, and the concentration of Pyr in the supernatant was measured using UV–Vis absorbance.

2.9. Adsorption and repolymerization of styrene (St) by hollow microspheres

A mixture of 5 mL of hollow PS_b^+ microspheres (h- PS_b^+) and 45 mL of deionized water was degassed under nitrogen at room temperature for 60 min. The solution was then heated to 80 °C after adding 0.8 mmol St and 0.007 mmol AIBA. Polymerization continued 24 h, followed by redispersion of the product in 50 mL deionized water for subsequent experiments.

2.10. Synthesis of raspberry-like PS@Au NPs nanoaggregates

In a centrifuge tube, 150 μL of Au NPs solution was mixed with 1 μL of PS microspheres stock solution. A visible colour change from ruby red to purple indicated self-assembly into raspberry-like PS@Au NPs nanoaggregates.

2.11. Calculation of adsorption capacity (q)

According to Beer-Lambert's law [44], which states that absorbance is directly proportional to concentration under specific conditions, measurements were taken at the maximum absorption wavelength of 334 nm. A standard curve was constructed based on the UV–Vis absorption spectra for Pyr ethanol solutions at different concentrations (Fig. S1a). Subsequently, UV–Vis absorption spectra of supernatants from both core–shell (cs-PS) and hollow polystyrene (h-PS) microspheres were measured (Fig. 1e), and concentrations were calculated by reference to the standard curve. The adsorption capacity (q) was calculated using the formula:

$$q = \frac{(c_0 - c_1)VM}{W}$$

Where q represents the adsorption capacity, c_0 and c_1 represent the initial and final Pyr concentrations respectively, V represents the solution volume, M represents the molar mass of Pyr, and W stands for adsorbent mass.

2.12. Calculation of Au NPs coverage rate (%) on PS microspheres

The coverage rate (%) was quantified by analyzing a 200 nm square area on each microsphere and calculating the number of Au NPs (N_{Au}) within it. The coverage rate (%) was calculated using the formula:

$$\% Coverage rate = \frac{S_{\textit{Au NPs}}}{S_{\textit{square area}}} = \frac{N_{\textit{Au NPs}} \times S_{\textit{single Au NP}}}{S_{\textit{square area}}} = \frac{N_{\textit{Au NPs}} \times \pi r^2}{l^2}$$

where r represents the radius of Au NPs, and l represents the length of the selected square area (l=200 nm).

$2.13. \ \ Calculation \ of \ interparticle \ distance \ of \ Au \ NPs \ on \ PS \ microspheres$

The interparticle distance of Au NPs on PS microspheres was determined based on the surface area occupied by each Au NP ($S_{occupied\ by\ each}$ Au NPs), calculated using the coverage ratio. Given that l=200 nm (the length of the selected square area of interest) and r is the radius of the Au NPs, the interparticle distance (nm) can be estimated using the formula:

Interparticle distance
$$(nm) = \sqrt{S_{occupied\ by\ each\ Au\ NPs}} - 2r$$

2.14. Numerical simulation of raspberry-like plasmonic nano-aggregates

The optical properties of raspberry-like plasmonic nano-aggregates were simulated using a commercial finite-difference time-domain (FDTD) software package (Ansys Lumerical). To match experimental conditions, 54 nm Au NPs were randomly distributed in varying numbers (ranging from 10 to 500) along the surface of a PS hollow

microsphere (inner diameter: 180 nm, outer diameter: 350 nm). The optical constant of Au was extracted from the literature [45], while the refractive index of PS was assumed to be 1.58 for the calculation simplicity. A linearly polarized plane wave (total-field scattered-field, TFSF source) was used as the illumination source, spanning a wavelength range of 400-800 nm. The source was positioned 100 nm from the nanoaggregate, which was centered inside a 500 nm \times 500 nm \times 500 nm simulation box. The incident wave propagated toward the core of the nanoaggregate, with the polarization angle set as depicted in the corresponding schematics. The inner refractive index of the PS hollow microsphere was assumed to be 1 (air), while the surrounding environment was modelled as water (refractive index: 1.33) to simplify the simulations. A perfectly matched layer (PML) with dimensions of 1500 nm \times 1500 nm \times 1500 nm was applied to mathematically simulate an infinite water environment, eliminating boundary interactions. For the 3D visualization of the optical near-field enhancement in the plasmonic nano-aggregate, the ratio of |E/E0| within the simulation domain at 633 nm was visualized using a scatter plot. The interval between scatter points was set to 5 nm, and 101 layers of 2D cross-sectional near-field distributions were computed along the nano-aggregate. To enhance the visibility of the near-field enhancement, regions where |E/E0| < 1.5were rendered transparent.

3. Results and discussion

3.1. Synthesis and adsorption properties of hollow microspheres

Fig. 1a illustrates the formation of linear PS seed microspheres through emulsion polymerization. These seed microspheres are utilized as sacrificial templates for the formation of functional core-shell microspheres with a crosslinked shell layer by incorporating monomers with distinct functional groups. TEM was employed to investigate morphological changes. Fig. 1b illustrates the morphology of the core-shell microspheres, whereas Fig. 1c displays the hollow microspheres created by removing the seed microsphere template. The unique hollow structure of these microspheres offers a significant advantage, as their cavities can effectively capture and enrich hydrophobic analytes in a hydrophobic microenvironment. This enhances the interaction between PAHs and the adsorption surface, facilitating π -cloud overlap between aromatic polystyrene and the adsorbed PAHs [42]. However, adsorption behavior may vary among different PAHs due to differences in their chemical structures. PAHs with lower hydrophobicity and molecular weight are expected to reach saturation faster than those with higher hydrophobicity and heavier molecular weight [46].

To demonstrate the enrichment capability for hydrophobic substances, core–shell and hollow microspheres were used to adsorb a 100 μM pyrene (Pyr) ethanol solution. The calculated adsorption capacities of Pyr for core–shell and hollow microspheres were 3.62 mg/g and 5.96 mg/g, respectively, highlighting the enhanced enrichment potential of hollow microspheres.

To further visualize adsorption of hydrophobic substances within the cavity of hollow microspheres, the hollow microspheres were dispersed in 45 mL of deionized water and heated to 80 $^{\circ}$ C after the adsorption of styrene (St) monomers. Unlike PAHs, St contains polymerizable double bonds, allowing the enrichment effect of hydrophobic substances to be visualized by TEM following thermally induced crosslinking. Fig. S1b indicates that the initially empty microsphere cavity became filled with PS as a result of the enriched St. This transformation from the core–shell microsphere structure (Fig. 1b) clearly demonstrates the effectiveness of the experimental approach in demonstrating the adsorption capability of hollow microspheres for trace amounts of St in aqueous solutions.

3.2. Synthesis of raspberry-like plasmonic nanoaggregates via aqueous self-assembly

The synthesis of Au NPs is achieved through the surface-catalyzed

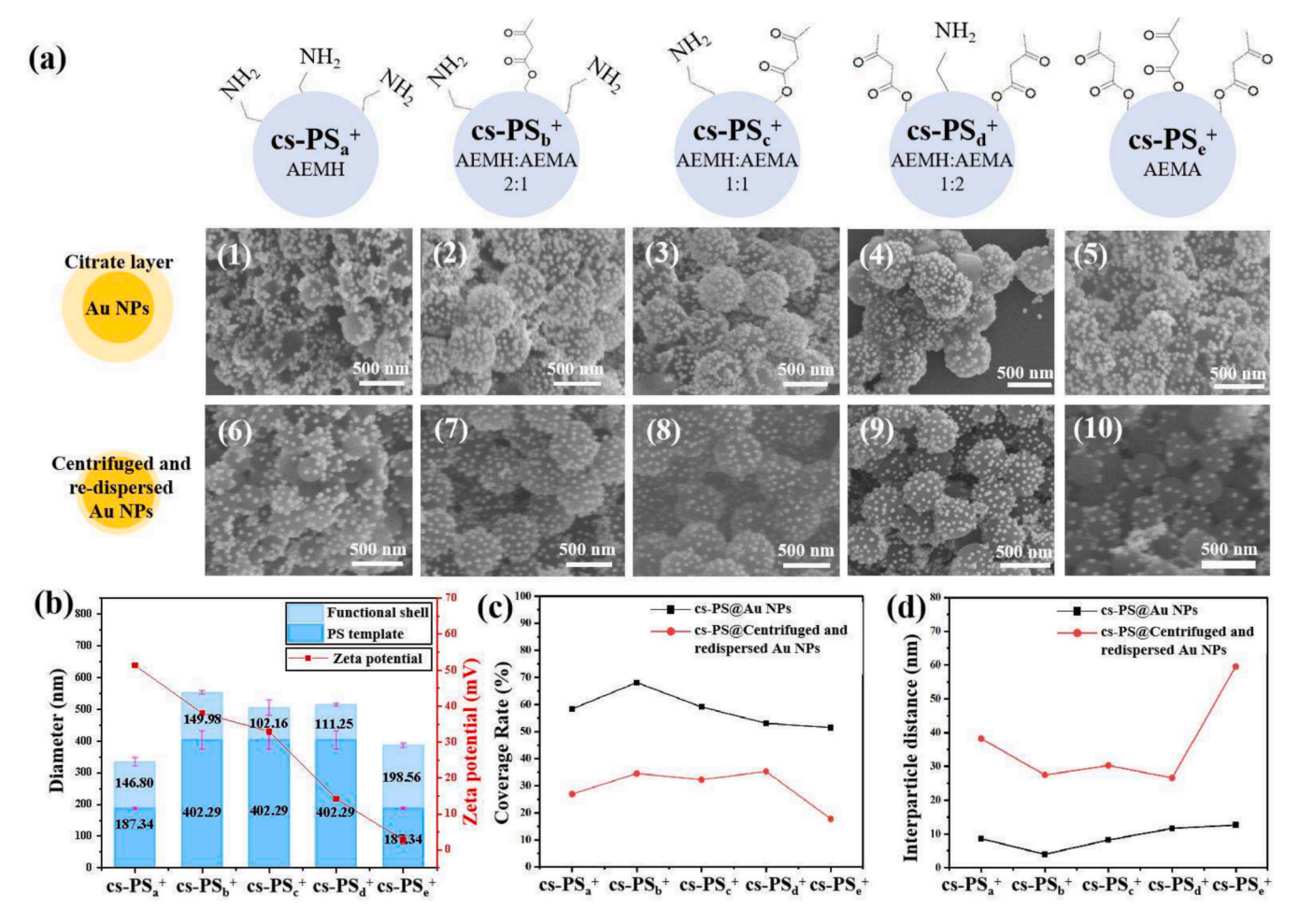


Fig. 2. (a 1–5) SEM images of nanoaggregates formed by Au NPs and five different core–shell microspheres (cs-PS $_a^+$, cs-PS $_c^+$, c

reduction of Au³⁺ by sodium citrate, resulting in a citrate capping layer that provides electrostatic stabilization to the Au NPs [43]. The UV–Vis spectrum (Fig. 1f, solid line) exhibits a localized surface plasmon resonance (LSPR) band centered around 529 nm, which aligns with the expected optical properties of Au NPs with a TEM-determined diameter of approximately 54 nm [47].

Upon introducing positively charged microspheres (PS⁺) into the Au NPs solution, a noticeable redshift in the LSPR peak occurs, shifting from 529 nm to 567 nm (Fig. 1f dotted line). This shift indicates significant plasmonic coupling and the formation of raspberry-like nanoaggregates. Based on Prashant's theory [48], the fractional shift in plasmon resonance wavelength, specifically when polarized along the interparticle axis, decreases exponentially with the interparticle gap. The observed redshift is attributed to the significant reduction in interparticle distance among Au NPs on the microspheres surface, leading to enhanced plasmonic interactions compared to isolated Au NPs.

Dynamic light scattering (DLS) measurements (Fig. 1g) further confirm the successful self-assembly of Au NPs onto PS $^+$ microspheres. The PS $^+$ microspheres exhibit an average hydrodynamic diameter of 356 \pm 4 nm, which increased to 459 \pm 5 nm after Au NPs attachment. This size increase validates the formation of stable raspberry-like nanoaggregates, reinforcing the effectiveness of the electrostatic self-assembly process.

The formation of these raspberry-like nanoaggregates arises from the interplay between electrostatic attraction and van der Waals forces among Au NPs, leading to localized clustering rather than a uniform

monolayer attachment. The structural arrangement enhances the SERS signal by increasing the number of plasmonic hotspots, although it may slightly reduce the accessible surface area for analyte binding.

To illustrate the role of electrostatic interactions between microspheres and Au NPs, negatively charged core–shell microspheres (PS') were synthesized and mixed with Au NPs (Fig. S2a). The mutual repulsion arising from identical negative charges Au NPs and PS' microspheres prevented the formation of raspberry-like nanoaggregates. This observation is supported by DLS measurements (Fig. S2b), which show no significant increase in the hydrodynamic diameter of PS' microspheres compared to monodisperse PS' microspheres, with a peak at 67 nm indicating the presence of isolated Au NPs. The UV–vis absorption spectrum confirms the absence of a redshift in the LSPR peak, further supporting the lack of nanoaggregate formation (Fig. S2c). Additionally, the appearance of a shoulder peak at 736 nm in the PS'@Au NPs spectrum suggests that negatively charged microspheres destabilize the solution, leading to uncontrolled aggregation of Au NPs.

3.3. Tunable surface coverage of raspberry-like plasmonic nanoaggregates

The synthesis of hollow raspberry-like plasmonic nanoaggregates involves creating a polymer shell layer composed of cross-linked poly [styrene-co-2-(acetoacetoxy)ethylmethacrylate-co-2-aminoethyl methacrylate hydrochloride] (PS-co-PAEMA-co-PAEMH) (Fig. 1a). The amino groups in AEMH facilitate electrostatic interactions with citrate-stabilized Au NPs, while the carbonyl groups from the PAEMA section

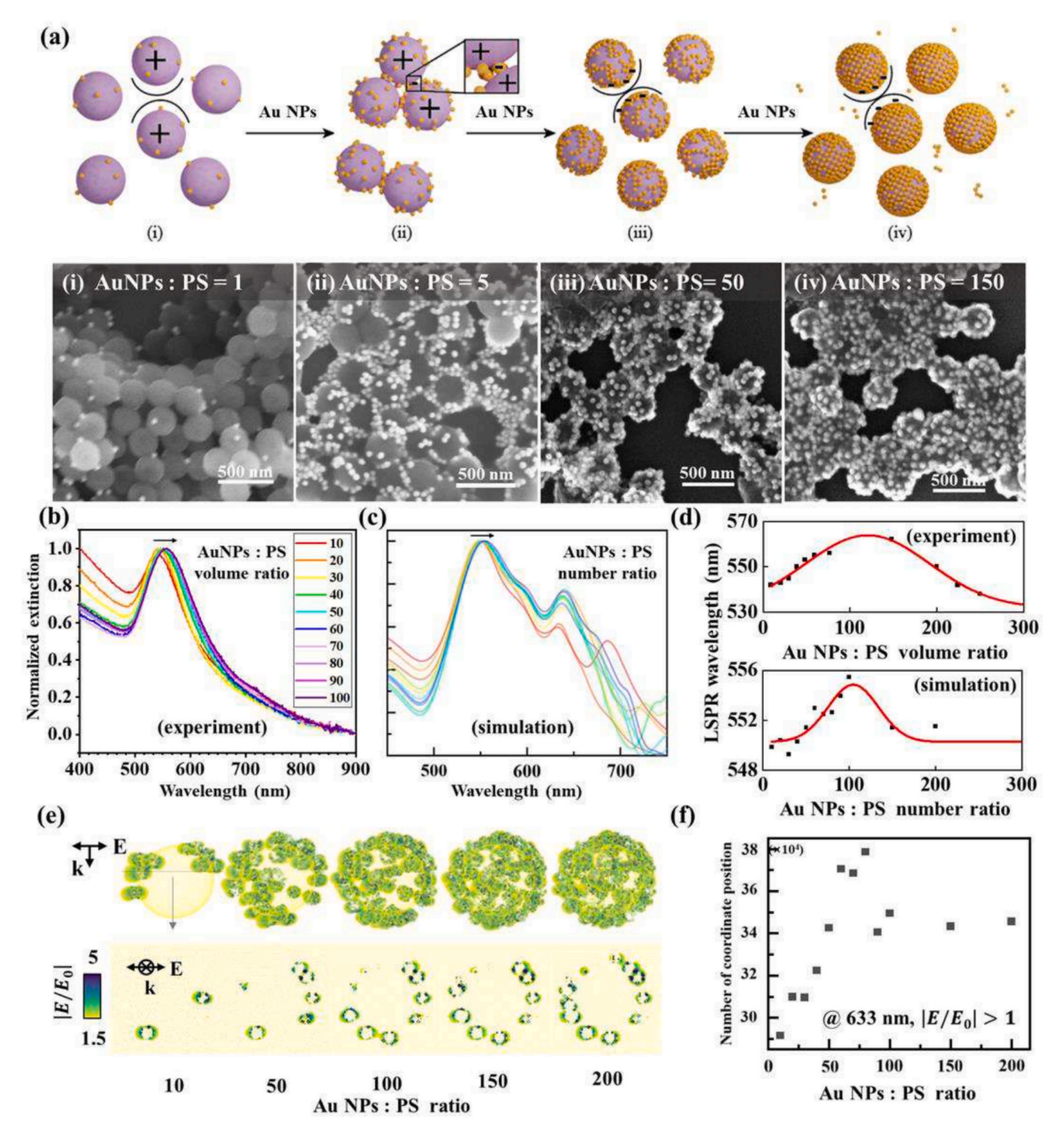


Fig. 3. Formation of hollow raspberry-like plasmonic nanoaggregates at different Au NPs: PS ratios. (a) Schematic illustration the formation process of hollow raspberry-like plasmonic nanoaggregates at Au NPs: PS volume ratios of 1, 5, 50, 150, along with the corresponding SEM images (scale bar: 500 nm); (b) Normalized UV–Vis spectrum showing the formation of hollow raspberry-like plasmonic nanoaggregates at various Au NP: PS volume ratios (experiment) and (c) corresponding simulations at various Au NP: PS number ratios;(d) LSPR peak wavelength of hollow raspberry-like plasmonic nanoaggregates as a function of the Au NPs: PS ratio (top: experimental results, bottom: numerical simulations). Red lines represent trend guidelines fitted with a Gaussian profile. (e) Optical near-field enhancements of hollow raspberry-like plasmonic nanoaggregates with varying numbers of Au NPs (10, 50, 100, 150, 200). The top panel shows 3D near-field distributions, while the bottom panel presents 2D cross-sectional views. (f) Corresponding number of spatial points within the simulation domain (500 nm \times 500 nm \times 500 nm, among a total of 1,030,301 points) where the near-field enhancement exceeds $|E/E_0| > 1$. (For interpretation of the references to color in this figure legend, the reader is referred to the web version of this article.)

regulate the density of these amino groups on the surface of the hollow microspheres. The attachment of 54 nm Au NPs to the microsphere surface can be adjusted by varying the content of functional monomers, as shown in the TEM images in Fig. 1d, which highlight both the Au NPs and the hollow cavity.

The optical characteristics of hollow raspberry-like plasmonic nanoaggregates are significantly influenced by the spacing between Au NPs on the microsphere surface. Tunable coverage of Au NPs was achieved by varying the molar ratio of functionalized monomers (AEMH and AEMA) in the hollow microsphere shell and adjusting the Au NPs: PS

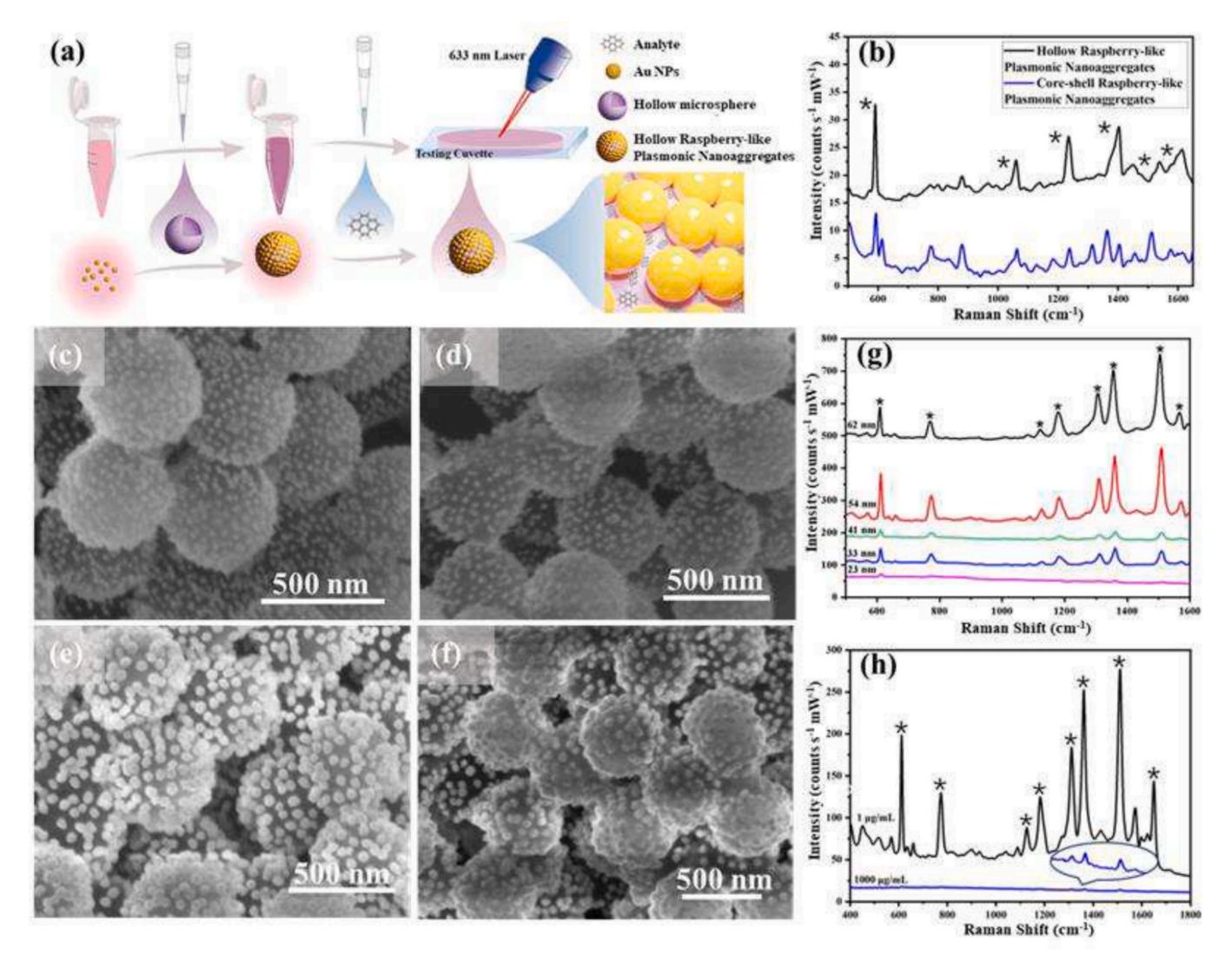


Fig. 4. SERS detection using hollow raspberry-like plasmonic nanoaggregates. (a) Schematic diagram of the detection process; (b) SERS spectrum of $100 \mu M$ Pyr using both core–shell and hollow raspberry-like plasmonic nanoaggregates as the SERS substrate; (c-f) SEM images of hollow raspberry-like plasmonic nanoaggregates (h-PS $_{\rm b}^+$) formed with Au NPs of different sizes (23 nm, 33 nm, 41 nm, 54 nm) (scale bar: 500 nm); (g) SERS spectrum of 1 $\mu g/mL$ R6G detected using hollow raspberry-like plasmonic nanoaggregates with different Au NPs sizes (23 nm, 33 nm, 41 nm, 54 nm, 62 nm); (h) Comparison of the SERS spectrum of 1 $\mu g/mL$ R6G (black line) using hollow raspberry-like plasmonic nanoaggregates (h-PS $_{\rm b}^+$ @Au NPs) with the normal Raman spectrum of $1000 \mu g/mL$ R6G (blue line). (For interpretation of the references to color in this figure legend, the reader is referred to the web version of this article.)

ratio during the self-assembly process. Amino groups, known for their favorable adsorption properties towards Au NPs [49,50], were incorporated into the microspheres using AEMH, which contains an acrylate unit capable of polymerizing with styrene and features an amino group for Au NPs binding. AEMA, extensively employed as a scaffold for transitional metal catalysts [51-53], indicates its potential for loading metal nanoparticles as well. Incorporating AEMA into microsphere synthesis results in a modest reduction in surface potential due to the presence of carbonyl groups at AEMA terminals. Unlike monomers with carboxylic acid groups [19], the carbonyl group in AEMA exerts a relatively weaker negative charge density, minimally affecting surface potential. Therefore, AEMA was selected to adjust the amino group density on microsphere surfaces to control over Au NPs surface coverage. This design strategy allowed for the synthesis of core-shell microspheres denoted as cs-PS $_a^+$ (AEMH), cs-PS $_b^+$ (AEMH: AEMA = 2:1), cs-PS_c⁺ (AEMH: AEMA = 1:1), cs-PS_d⁺ (AEMH: AEMA = 1:2) and cs-PS_c⁺ (AEMA). cs-PS $_a^+$ and cs-PS $_e^+$ represent microspheres predominantly featuring amino and dense carbonyl groups on their surfaces, respectively. The density of amino groups on the surface of the hollow microspheres was monitored by ζ - potential measurements, a reliable

method for evaluating PS microsphere surface chemistry [54]. As illustrated in Fig. 2b, cs-PS $_a^+$ exhibited an average ζ -potential of + 51.26 mV, which reduced to + 2.73 mV in cs-PS $_e^+$ with higher AEMA content, demonstrating effective control over surface potential by adjusting the ratio of functionalized monomer.

Au NPs successfully bound to the surface of all five cs-PS⁺ microspheres (Fig. 2a 1-5), albeit with varying degrees of coverage. Analysis of SEM images (Fig. 2a 1-5) allowed for the calculation of coverage rate and interparticle distance for each of the five cs-PS⁺ microspheres. Surprisingly, cs-PS⁺ microspheres, with a small number of carbonyl functional groups, exhibited the highest coverage at 68.1 %, which gradually decreased from cs-PS⁺ (68.1 %) to cs-PS⁺ (51.5 %). Notably, cs-PS⁺ nanoaggregates achieved a minimum interparticle distance of approximately 4 nm, demonstrating dense packing facilitated by AEMA's uniform distribution of surface amino groups. Fig. 2a-1 illustrates microspheres with AEMA addition, while Fig. 2a 2-5 show microspheres with AEMA. The additional of the carbonyl functionalized monomer (AEMA) resulted in a more uniform distribution of surface amino groups, enhancing the uniformity and density of Au NPs coverage. This finding aligns with existing literature highlighting

AEMA's role in improving particle stability during emulsion polymerization [55].

To validate the role of citrate on Au NP surface interactions during the self-assembly of raspberry-like nanoaggregates, a centrifugation and redispersion cycle was performed to reduce the effective thickness of the citrate layer on Au NPs [56]. Fig. 2a 6–10 shows the formation of raspberry-like nanoaggregates using centrifuged and re-dispersed Au NPs with the five different microspheres. The diminished citrate layer on the Au NPs surface weakened electrostatic interactions, resulting in an overall reduction in coverage. Additional investigations varying sodium citrate concentrations (1.2 mM, 2.4 mM, 3.2 mM and 4.0 mM) directly added to the centrifuged and redispersed Au NPs solution (Fig. S3) showed no significant improvement in surface coverage. This underscores the necessity of citrate during Au NPs synthesis for effective oxidized and stably attachment to their surface.

Adjusting the Au NPs: PS ratio allows precise control over the coverage percentage of nanoaggregates. The h-PS_b⁺ microspheres, with an AEMH: AEMA ratio of 2:1, exhibited optimal performance in forming hollow raspberry-like nanoaggregates (henceforth abbreviated as PS in the following description). We investigated the impact of the Au NPs: PS ratio on solution stability and nanoaggregates morphology by varying the PS content while keeping a constant amount of Au NPs, evaluating coverage and stability. Hollow raspberry-like plasmonic nanoaggregates were successfully formed across Au NPs: PS ratios ranging from 1 to 1000. UV–Vis spectra recorded after 5 min of self-assembly (Fig. 3b-d) revealed the LSPR wavelength of hollow raspberry-like plasmonic nanoaggregates at various Au NPs: PS ratio.

At Au NPs: PS ≤ 1 , PS microspheres dominated as the major component (Fig. 3 a-i). The presence of Au NPs minimally affected the solution's ionic strength, enabling robust electrostatic repulsion among PS microspheres. A slight increase in Au NPs content disrupted the electrostatic balance between PS-PS repulsion and Au NP-PS attraction, leading to extensive aggregation and rapid precipitation within 10 min (Fig. 3 a-ii).

In the range of $10 \leq Au$ NPs: PS ≤ 100 , increased Au NPs content enhanced surface coverage on PS microspheres, maintaining stability through electrostatic repulsion between Au NPs surface and adjacent PS microspheres. This reduced the adhesion of individual Au NPs to multiple PS microspheres, maintaining colloidal stability for up to 30 min without precipitation. A redshift in wavelength indicated reduced spacing between adjacent Au NPs on the PS surface (Fig. 3 a-iii).

Upon reaching an Au NPs: PS volume ratio of 100–150, the wavelength experienced the furthest redshift at 562 nm (Fig. 3b), indicating saturated Au NPs coverage on PS surface. Further increases in Au NPs: PS reduced the redshift due to isolated Au NPs, indicating saturation of Au NPs coverage. Fig. S4 presents the extinction LSPR peaks of hollow raspberry-like plasmonic nanoaggregates, which reflect the extent of plasmonic coupling between Au NPs within the nanoaggregates. The most pronounced redshift occurs at a volume ratio of 150, signifying the strongest plasmonic interactions.

This redshift in plasmonic resonances is further supported by numerical simulations (Fig. 3c). As the Au NPs: PS number ratio increases from 10 to 100, the plasmonic resonance redshifts. However, beyond a ratio of 100, a blueshift is observed, consistent with experimental results. This behavior arises from the finite density of optical hotspots (near-field enhancements, Fig. 3e), which is constrained by the maximum number of Au NPs that can physically attach to the available PS microsphere surface.

As shown in Fig. 3d, both experiment and simulation results align, demonstrating that the LSPR peak can be precisely tuned by adjusting the Au NPs: PS ratio. A more detailed visualization of near-field distributions is provided in Fig. S5, showing 2D cross-sectional slices of optical near-field enhancements at different sections of each raspberry-like plasmonic nanoaggregate. Notably, an analysis of coordinate positions with near-field enhancements exceeding the incident field at 633 nm (the laser wavelength used for SERS) reveals that number ratios above

80 generate the highest hotspot density per aggregate (Fig. 3f). This configuration maximizes SERS signal enhancement, making it the most effective structure for achieving strong Raman signals.

To experimentally validate the optimal Au NPs to PS ratio for SERS applications, volume ratios ranging from 50 to 1000 were evaluated using 1 $\mu g/mL$ R6G. As show in Fig. S6, the strongest signal was observed at a volume ratio of 150, aligning with maximum redshift observed in Fig. S4. Therefore, this ratio was selected for subsequently SERS measurements. Additionally, Inductively Coupled Plasma-Mass Spectrometry (ICP-MS) and Energy Dispersive Spectroscopy (EDS) analyses were conducted to determine the actual mass ratio of Au NPs: PS (Fig. S7). The ICP-MS data indicate an Au mass concentration of 0.205 g/L, confirming an actual mass ratio of Au NPs: PS of approximately 153:1.

3.4. SERS detection of PAHs using hollow raspberry-like plasmonic nanoaggregates

In the detection procedure, analytes are introduced into the mixture, followed by SERS detection in a quartz cuvette (Fig. 4a). Compared to Au NPs [57–61], the hollow raspberry-like plasmonic nanoaggregates exhibit significantly reduced uncontrolled aggregation upon analytes addition over several hours, ensuring stable SERS signals throughout the testing period (Fig. S8a). The relative standard deviation (RSD) of the h-PS $_{\rm b}^+$ @Au NPs remained at 1.16 % over 90 days (Fig. S8b), demonstrating excellent long-term storage stability and readiness for rapid use. Additionally, SERS analysis of the hollow raspberry-like plasmonic nanoaggregates reveals minimal background noise and no interference peaks in the Raman spectrum (Fig. S8c). The use of a liquid-based SERS substrate ensures a homogeneous distribution of analytes. Analyzing 10 randomly selected points from a 1 µg/mL of Rhodamine 6G (R6G) solution confirms high reproducibility, with an RSD value of 5.62 % (Fig. S8d).

To assess the impact of cavity enrichment on SERS enhancement, we compared the adsorption characteristics and SERS performance of hollow and core–shell raspberry-like plasmonic nanoaggregates. Both types were tested under identical conditions by adsorbing 100 μM Pyr (Fig. S9). The hollow nanoaggregates exhibited a 7.38 % higher adsorption rate than the core–shell structures, confirming that the cavity design improves adsorption efficiency for hydrophobic analytes. As a result, the detection of 100 μM Pyr showed a 2-fold amplification in the SERS signal for hollow nanoaggregates (Fig. 4b), highlighting the impact of enrichment effects. Although the inner cavities are not directly adjacent to the hotspots, they influence the local concentration of analyte across the entire nanoaggregates, including the hotspot regions where most SERS signals originate.

The size and morphology of Au NPs significantly affect Raman characteristics. In this study, four different hollow raspberry-like nanoaggregates (h-PSh-@Au NPs) were characterized by SEM, revealing that Au NPs of different particle sizes can form raspberry-like nanoaggregates with hollow PS microspheres (Fig. 4c-f). Previous studies simulating the electric field enhancement of Au NPs of different sizes at 633 nm demonstrated that Au NPs around 50 nm exhibit the strongest field enhancement, which directly correlates with superior SERS performance [62]. Using R6G as a Raman probe, we systematically examined the relationship between SERS properties and Au NPs size (ranging from 23 nm to 62 nm) in these nanoaggregates. Our experimental results confirm that Au NPs around 50 nm provide the optimal electric field enhancement (Fig. 4g). Specifically, analysis of two characteristic peaks of R6G at 1361 cm⁻¹ and 1508 cm⁻¹ revealed enhancement factor (EF) of 1.02×10^5 and 1.48×10^5 , respectively, underscoring the significant signal enhancement achieved through the raspberry-like nanostructures (Fig. 4h).

The hydrophobic cavities within the hollow raspberry-like plasmonic nanoaggregates facilitate the successful detection of ultra-low concentrations of PAHs, such as pyrene (Pyr), fluoranthene (Flu) and benzo[a]

Table 1
SERS detection of Pyr, Flu and BaA, and fitting relationships.

Analytes	LOD	Fitting relationship Low concentration	Broad concentration
Pyr	$\begin{array}{c} 4\times 10^{\text{-8}} \\ M \end{array}$	$\begin{array}{l} 0.31.0~\mu\text{M} \\ y = \text{-}0.3301 + 3.2070x~(\text{R}^2 \\ = 0.9912) \end{array}$	$0.04100~\mu\text{M}$ Logistic fitting (R ² = 0.9988)
Flu	6×10^{-7} M	$\begin{aligned} &0.61.0~\mu\text{M}\\ &y=\text{-}0.5629+1.8145x~(\text{R}^2\\ &=0.9675) \end{aligned}$	$\begin{array}{l} 1100~\mu\text{M} \\ y = 2.3401 + 0.1131x~(\text{R}^2 \\ = 0.9995) \end{array}$
BaA	$\begin{array}{c} 4\times 10^{\text{-}7}\\ M \end{array}$	$\begin{aligned} &0.41.0~\mu\text{M}\\ &y=\text{-0.2710}+1.3930x~(R^2\\ &=0.9929) \end{aligned}$	$\begin{array}{l} 180 \; \mu M \\ y = 1.0240 + 0.1365x \; (R^2 \\ = 0.9926) \end{array}$

anthracene (BaA). Table 1 and Fig. 5 show the ultra-low detection limit for these PAHs, demonstrating the combined effects of cavity enrichment and built-in hotspots. Specifically, detection limits were determined to be 4×10^{-8} M for Pyr, 6×10^{-7} M for Flu and 4×10^{-7} M for BaA. Existing Pyr detection methods often rely on analyte-induced aggregation strategies [60,61], which compromise solution stability and repeatability (Table S1). Moreover, alternative enhancements approaches using pillar[5] arene [63], β -cyclodextrin [64], graphene oxide

(GO) [65], alkyl chain [66] and humic acids [67] require complex modification process. While the coffee ring effect [68] induced by evaporation can efficiently concentrate analytes, it inevitably reduce substrate uniformity, further limiting reproducibility. In contrast, our hollow raspberry-like plasmonic nanoaggregates achieves ultra-low LOD while ensuring remarkable repeatability due to their stable, solution-based SERS substrate, significantly enhances reliability and consistency in detection (Table S1 - S3).

To further understand the detection mechanism, we analyzed the relationship between analyte concentration and Raman intensity revealing distinct behaviors for different PAHs. At low concentrations, Raman intensity exhibited a linear relationship with analyte concentration. However, as the concentration increased, Pyr exhibited a logarithmic trend, indicating a diminishing rate of peak intensity increase due to the fixed number of hotspots. At low analyte concentrations, analyte molecules efficiently access these hotspots, resulting in a strong signal. However, as concentration increases, additional molecules accumulate at the periphery of saturated hotspots, leading to reduced signal amplification. Conversely, Flu and BaA showed segmented trends across the measurement range, with Flu showing two distinct linear relationships. The slope in the higher concentration range was more

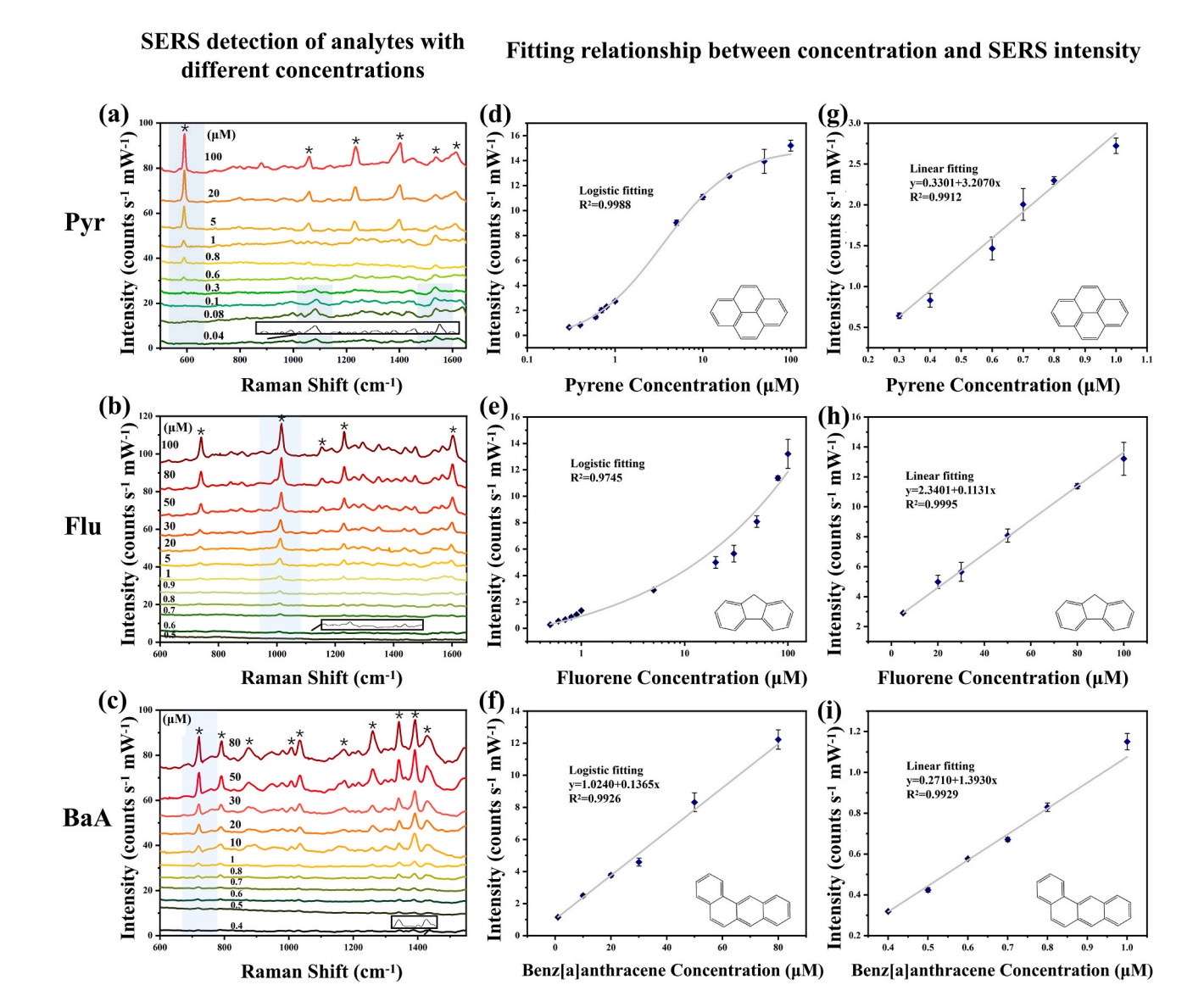


Fig. 5. Raman spectrum of analytes (Pyr, Flu, BaA), (a-c) concentration-dependent SERS signal of analytes using hollow raspberry-like plasmonic nanoaggregates (h-PSh@Au NPs) as the SERS substrate, and (d-i) fitting relationships for SERS intensity at characteristic Raman shift.

Table 2Detection of PAHs in environmental water.

Samples	Analytes/ Add (μM)	Pyr		Flu		BaA	
		Recovery (%)	RSD (%)	Recovery (%)	RSD (%)	Recovery (%)	RSD (%)
The Yellow River water	1	111.74	7.50	112.34	4.78	105.26	8.93
	5	101.89	3.85	107.36	2.41	99.60	0.11
	10	92.31	5.31	105.50	1.96	110.57	4.37
Tap water	1	105.81	5.05	101.84	4.90	89.33	5.30
	5	98.08	1.83	100.38	4.44	90.68	2.83
	10	90.40	4.93	94.20	1.73	106.47	3.09

than an order of magnitude smaller than in lower concentrations, highlighting the higher sensitivity of SERS for detecting trace number of analytes.

To assess the capability of our SERS substrate in distinguishing individual PAHs within a mixture, we conducted experiments using an aqueous solution containing equal concentrations (50 μM) of Pyr, Flu, and BaA. By selecting distinct, non-interfering Raman characteristic peaks at 592, 740, and 714 cm $^{-1}$ for Pyr, Flu, and BaA, respectively, we successfully identified each PAHs within the mixture without spectral interference (Fig. S10). These results demonstrate that our sensor effectively differentiates individual PAHs based on their unique Raman spectral signatures.

3.5. SERS detection of PAHs in environmental water using hollow raspberry-like plasmonic nanoaggregates

To evaluate the effectiveness of our nanoaggregates as a SERS substrate for detecting PAHs in environmental water samples, we spiked the Yellow River water and tap water with 1, 5, and $10\,\mu\text{M}$ concentrations of Pyr, Flu and BaA. SERS analysis of the unspiked environmental water samples revealed no detectable PAHs, confirming that the original water samples were free of these compounds (Fig. S11a). Follow spiking, we calculated the recoveries of PAHs using characteristic fitting equations (Fig. S11 b-d), with detailed results in Table 2. The recoveries for Pyr, Flu, and BaA ranged from 90 % to 115 %, demonstrating the method's high accuracy. These findings confirm that our approach is highly effective for detecting PAHs in environmental water samples.

4. Conclusions

In summary, the hollow PS@Au NPs plasmonic nanoaggregates synthesized in this study demonstrate dual functionality, enabling both the enrichment and detection of analytes. Their application in surfaceenhanced Raman spectroscopy (SERS) in solution form effectively overcomes the inconsistencies associated with solid SERS substrates and significantly enhances the detection of hydrophobic analytes, such as polycyclic aromatic hydrocarbons (PAHs), by leveraging hollow polymer microspheres as the adsorption material. The detection limits for pyrene (Pyr), fluorene (Flu) and benzo[a]anthracene (BaA) were determined to be 4×10^{-8} M, 6×10^{-7} M and 4×10^{-7} M, respectively. This approach was successfully applied to environmental water samples, including the Yellow River water and tap water, demonstrating high sensitivity and accuracy in PAHs detection, thereby highlighting the potential of these nanoaggregates for identifying hydrophobic analytes at ultra-low concentrations. Additionally, the capacity to control the size of the assembled metal nanoparticles and adjust the interstitial gaps within the raspberry-like structure enhances the accessibility of active sites. This study highlights the capabilities of hollow raspberry-like plasmonic nanoaggregates for quantitative analysis of PAHs, thereby broadening the use of advanced nanomaterials in monitoring environmental water quality.

CRediT authorship contribution statement

Huimin Xie: Writing – original draft, Methodology, Formal analysis, Data curation. Shuyu Zhu: Writing – original draft, Methodology, Formal analysis, Data curation. Jingwen Cao: Writing – review & editing, Data curation. JuHyeong Lee: Data curation. Yidan Yin: Writing – review & editing. Deyue Zhou: Writing – review & editing. Jing Yan: Writing – review & editing. Hyeon-Ho Jeong: Data curation. Tung-Chun Lee: Writing – review & editing, Conceptualization. Yuewen Zhang: Writing – review & editing, Supervision, Project administration, Funding acquisition, Formal analysis, Conceptualization. Qiaosheng Pu: Conceptualization. Yang Lan: Writing – review & editing, Supervision, Formal analysis, Conceptualization.

Declaration of competing interest

The authors declare that they have no known competing financial interests or personal relationships that could have appeared to influence the work reported in this paper.

Acknowledgements

Y. Z. acknowledges the support of the National Natural Science Foundation of China (Grant No. 22204065) and the Natural Science Foundation of Gansu Province, China (Grant No. 21JR7RA462).

Appendix A. Supplementary data

Supplementary data to this article can be found online at https://doi. org/10.1016/j.cej.2025.161872.

Data availability

Data will be made available on request.

References

- [1] M. Liu, H. Zheng, M. Cai, K.M.Y. Leung, Y. Li, M. Yan, Z. Zhang, K. Zhang, M. Chen, H. Ke, Ocean Stratification Impacts on Dissolved Polycyclic Aromatic Hydrocarbons (PAHs): From Global Observation to Deep Learning, Environ. Sci. Tech. 57 (46) (2023) 18339–18349, https://doi.org/10.1021/acs.est.3c03237.
- [2] J. Xie, L. Tao, Q. Wu, S. Lei, T. Lin, Environmental profile, distributions and potential sources of halogenated polycyclic aromatic hydrocarbons, J. Hazard. Mater. 419 (2021) 126164, https://doi.org/10.1016/j.jhazmat.2021.126164.
- [3] M. Moradi, H. Hung, J. Li, R. Park, C. Shin, N. Alexandrou, M.A. Iqbal, M. Takhar, A. Chan, J.R. Brook, Assessment of Alkylated and Unsubstituted Polycyclic Aromatic Hydrocarbons in Air in Urban and Semi-Urban Areas in Toronto, Canada, Environmental Science & Technology 56 (5) (2022) 2959–2967, https://doi.org/ 10.1021/acs.est.lc04299.
- [4] X. Li, Y. Lu, Y. Shi, P. Wang, X. Cao, H. Cui, M. Zhang, D. Du, Effects of urbanization on the distribution of polycyclic aromatic hydrocarbons in China's estuarine rivers, Environ. Pollut. 301 (2022) 119001, https://doi.org/10.1016/j. envpol.2022.119001.
- [5] G.L. Daly, F. Wania, Organic Contaminants in Mountains, Environ. Sci. Tech. 39 (2) (2005) 385–398, https://doi.org/10.1021/es048859u.
- [6] P. Karimi, K.O. Peters, K. Bidad, P.T. Strickland, Polycyclic aromatic hydrocarbons and childhood asthma, Eur. J. Epidemiol. 30 (2) (2015) 91–101, https://doi.org/ 10.1007/s10654-015-9988-6.
- [7] O. Alshaarawy, H.A. Elbaz, M.E. Andrew, The association of urinary polycyclic aromatic hydrocarbon biomarkers and cardiovascular disease in the US population,

- Environ. Int. 89–90 (2016) 174–178, https://doi.org/10.1016/j.
- [8] S.X. Naughton, S. Westfall, G.M. Pasinetti, Diesel exhaust particle role on gut microbiome and onset of Alzheimer disease neuroinflammation, Alzheimers Dement. 16 (S10) (2020) e046266, https://doi.org/10.1002/alz.046266.
- [9] G.-L. Zhang, M. Zhang, Q. Shi, Z. Jiang, L. Tong, Z. Chen, B. Tang, In Situ Construction of COF-Based Paper Serving as a Plasmonic Substrate for Enhanced PSI-MS Detection of Polycyclic Aromatic Hydrocarbons, ACS Appl. Mater. Interfaces 13 (36) (2021) 43438–43448, https://doi.org/10.1021/ acsami.1c13860.
- [10] J. Yi, E.-M. You, R. Hu, D.-Y. Wu, G.-K. Liu, Z.-L. Yang, H. Zhang, Y. Gu, Y.-H. Wang, X. Wang, H. Ma, Y. Yang, J.-Y. Liu, F.R. Fan, C. Zhan, J.-H. Tian, Y. Qiao, H. Wang, S.-H. Luo, Z.-D. Meng, B.-W. Mao, J.-F. Li, B. Ren, J. Aizpurua, V. A. Apkarian, P.N. Bartlett, J. Baumberg, S.E.J. Bell, A.G. Brolo, L.E. Brus, J. Choo, L. Cui, V. Deckert, K.F. Domke, Z.-C. Dong, S. Duan, K. Faulds, R. Frontiera, N. Halas, C. Haynes, T. Itoh, J. Kneipp, K. Kneipp, E.C. Le Ru, Z.-P. Li, X.Y. Ling, J. Lipkowski, L.M. Liz-Marzan, J.-M. Nam, S. Nie, P. Nordlander, Y. Ozaki, R. Panneerselvam, J. Popp, A.E. Russell, S. Schluecker, Y. Tian, L. Tong, H. Xu, Y. Xu, L. Yang, J. Yao, J. Zhang, Y. Zhang, Y. Zhang, B. Zhao, R. Zenobi, G. C. Schatz, D. Graham, Z.-Q. Tian, Surface-enhanced Raman spectroscopy: a half-century historical perspective, Chem. Soc. Rev. 54 (3) (2024) 1453–1551, https://doi.org/10.1039/ddcs00883a.
- [11] A.M. Dowgiallo, D.A. Guenther, Determination of the Limit of Detection of Multiple Pesticides Utilizing Gold Nanoparticles and Surface-Enhanced Raman Spectroscopy, J. Agric. Food Chem. 67 (46) (2019) 12642–12651, https://doi.org/ 10.1021/acs.jafc.9b01544
- [12] M. Azubel, R.D. Kornberg, Synthesis of Water-Soluble, Thiolate-Protected Gold Nanoparticles Uniform in Size, Nano Lett. 16 (5) (2016) 3348–3351, https://doi. org/10.1021/acs.nanolett.6b00981.
- [13] M. Ha, J.-H. Kim, M. You, Q. Li, C. Fan, J.-M. Nam, Multicomponent Plasmonic Nanoparticles: From Heterostructured Nanoparticles to Colloidal Composite Nanostructures, Chem. Rev. 119 (24) (2019) 12208–12278, https://doi.org/ 10.1021/acs.chemrev.9b00234.
- [14] K.L. Wustholz, A.-I. Henry, J.M. McMahon, R.G. Freeman, N. Valley, M.E. Piotti, M. J. Natan, G.C. Schatz, R.P. Van Duyne, Structure—Activity Relationships in Gold Nanoparticle Dimers and Trimers for Surface-Enhanced Raman Spectroscopy, J. Am. Chem. Soc. 132 (31) (2010) 10903–10910, https://doi.org/10.1021/ia104174m.
- [15] C.E. Talley, J.B. Jackson, C. Oubre, N.K. Grady, C.W. Hollars, S.M. Lane, T. R. Huser, P. Nordlander, N.J. Halas, Surface-Enhanced Raman Scattering from Individual Au Nanoparticles and Nanoparticle Dimer Substrates, Nano Lett. 5 (8) (2005) 1569–1574. https://doi.org/10.1021/n1050928v.
- [16] P. Wang, Y. Zhou, Y. Zhou, Y. Wen, F. Wang, H. Yang, In-situ growth of raspberry-like silver composites for Raman detection of acrylamide, Sens. Actuators B 243 (2017) 856–862, https://doi.org/10.1016/j.snb.2016.12.056.
- [17] M.J. Jeon, X. Ma, J.U. Lee, H. Roh, C.C. Bagot, W. Park, S.J. Sim, Precisely Controlled Three-Dimensional Gold Nanoparticle Assembly Based on Spherical Bacteriophage Scaffold for Molecular Sensing via Surface-Enhanced Raman Scattering, J. Phys. Chem. C 125 (4) (2021) 2502–2510, https://doi.org/10.1021/ acs.incc.0r08800
- [18] Y. Rong, L. Zhang, Z. Liu, L. Dai, Y. Huang, T. Chen, Facile Synthesis of Uniform Raspberry-Like Gold Nanoparticles for High Performance Surface Enhanced Raman Scattering, J. Nanosci. Nanotechnol. 16 (6) (2016) 5683–5688, https://doi.org/ 10.1166/jnn.2016.11723.
- [19] S.A. Belhout, F.R. Baptista, S.J. Devereux, A.W. Parker, A.D. Ward, S.J. Quinn, Preparation of polymer gold nanoparticle composites with tunable plasmon coupling and their application as SERS substrates, Nanoscale 11 (42) (2019) 19884–19894, https://doi.org/10.1039/C9NR05014K.
- [20] A. Le Beulze, S. Gomez-Grana, H. Gehan, S. Mornet, S. Ravaine, M. Correa-Duarte, L. Guerrini, R.A. Alvarez-Puebla, E. Duguet, E. Pertreux, A. Crut, P. Maioli, F. Vallee, N. Del Fatti, O. Ersen, M. Treguer-Delapierre, Robust raspberry-like metallo-dielectric nanoclusters of critical sizes as SERS substrates, Nanoscale 9 (17) (2017) 5725–5736, https://doi.org/10.1039/c7nr00969k.
- [21] E. Cloutis, P. Szymanski, D. Applin, D. Goltz, Identification and discrimination of polycyclic aromatic hydrocarbons using Raman spectroscopy, Icarus 274 (2016) 211–230, https://doi.org/10.1016/j.icarus.2016.03.023.
- [22] B. Mehta, M. Mehta, Organic chemistry, PHI Learning Pvt. Ltd., 2015.
- [23] A. Sharma, S.J.I.N.-Y. Schulman, Introduction to Fluorescence Spectroscopy. John Willey & Sons, (1999).
- [24] M. Signorile, F. Bonino, A. Damin, S. Bordiga, In Situ Resonant UV-Raman Spectroscopy of Polycyclic Aromatic Hydrocarbons, J. Phys. Chem. C 119 (21) (2015) 11694–11698, https://doi.org/10.1021/acs.jpcc.5b02209.
- [25] J. Ferguson, L.W. Reeves, W.G. Schneider, Vapor absorption spectra and oscillator strengths of naphthalene, anthracene, and pyrene, Can. J. Chem. 35 (1957) 1117–1136, https://doi.org/10.1139/v57-152.
- [26] H.K. Lee, Y.H. Lee, C.S.L. Koh, P.-Q. Gia Chuong, X. Han, C.L. Lay, H.Y.F. Sim, Y.-C. Kao, Q. An, X.Y. Ling, Designing surface-enhanced Raman scattering (SERS) platforms beyond hotspot engineering: emerging opportunities in analyte manipulations and hybrid materials, Chem. Soc. Rev. 48 (3) (2019) 731–756, https://doi.org/10.1039/c7cs00786h.
- [27] M. Zhang, X. Zhang, Y.-E. Shi, Z. Liu, J. Zhan, Surface enhanced Raman spectroscopy hyphenated with surface microextraction for in-situ detection of polycyclic aromatic hydrocarbons on food contact materials, Talanta 158 (2016) 322–329, https://doi.org/10.1016/j.talanta.2016.05.069.
- [28] M. Qiu, L. Tang, J. Wang, Q. Xu, S. Zheng, S. Weng, SERS with Flexible β -CD@ AuNP/PTFE Substrates for In Situ Detection and Identification of PAH Residues on

- Fruit and Vegetable Surfaces Combined with Lightweight Network, Foods 12 (16) (2023) 3096, https://doi.org/10.3390/foods12163096.
- [29] L. Guerrini, J.V. Garcia-Ramos, C. Domingo, S. Sanchez-Cortes, Sensing Polycyclic Aromatic Hydrocarbons with Dithiocarbamate-Functionalized Ag Nanoparticles by Surface-Enhanced Raman Scattering, Anal. Chem. 81 (3) (2009) 953–960, https://doi.org/10.1021/ac801709e.
- [30] W.-I.-K. Chio, H. Xie, Y. Zhang, Y. Lan, T.-C. Lee, SERS biosensors based on cucurbituril-mediated nanoaggregates for wastewater-based epidemiology, TrAC Trends Anal. Chem. 146 (2022) 116485, https://doi.org/10.1016/j. trac.2021.116485.
- [31] F. Wang, Y. Zheng, J. Qiu, S. Liu, Y. Tong, F. Zhu, G. Ouyang, Graphene-based metal and nitrogen-doped carbon composites as adsorbents for highly sensitive solid phase microextraction of polycyclic aromatic hydrocarbons, Nanoscale 10 (21) (2018) 10073–10078, https://doi.org/10.1039/c8nr01910j.
- [32] J. Munoz, A. Campos-Lendinez, N. Crivillers, M. Mas-Torrent, Selective Discrimination of Toxic Polycyclic Aromatic Hydrocarbons in Water by Targeting π-Stacking Interactions, ACS Appl. Mater. Interfaces 12 (23) (2020) 26688–26693, https://doi.org/10.1021/acsami.0c05557.
- [33] T.-H. Park, D.-J. Jang, Laser-induced fabrication of porous gold nanoshells, Nanoscale 10 (43) (2018) 20108–20112, https://doi.org/10.1039/C8NR04617D.
- [34] P. Ye, W. Xin, I.M. De Rosa, Y. Wang, M.S. Goorsky, L. Zheng, X. Yin, Y.-H. Xie, One-Pot Self-Templated Growth of Gold Nanoframes for Enhanced Surface-Enhanced Raman Scattering Performance, ACS Appl. Mater. Interfaces 12 (19) (2020) 22050–22057, https://doi.org/10.1021/acsami.0c04777.
- [35] S. Jeong, M.-W. Kim, Y.-R. Jo, N.-Y. Kim, D. Kang, S.Y. Lee, S.-Y. Yim, B.-J. Kim, J. H. Kim, Hollow Porous Gold Nanoshells with Controlled Nanojunctions for Highly Tunable Plasmon Resonances and Intense Field Enhancements for Surface-Enhanced Raman Scattering, ACS Appl. Mater. Interfaces 11 (47) (2019) 44458–44465, https://doi.org/10.1021/acsami.9b16983.
- [36] D.M. Vriezema, M. Comellas Aragonès, J.A.A.W. Elemans, J.J.L.M. Cornelissen, A. E. Rowan, R.J.M. Nolte, Self-Assembled Nanoreactors, Chemical Reviews 105(4) (2005) 1445–1490, https://doi.org/10.1021/cr0300688.
- [37] S.M. Leeder, M.R. Gagné, Fluorophobic Effect Promotes Partitioning of Organics into Macroporous Organic Polymers: A Method for Achieving High Local Concentrations, J. Am. Chem. Soc. 125 (30) (2003) 9048–9054, https://doi.org/ 10.1021/ja03535558.
- [38] D. Yao, Y. Wang, K. Hassan-Legault, A. Li, Y. Zhao, J. Lv, S. Huang, X. Ma, Balancing Effect between Adsorption and Diffusion on Catalytic Performance Inside Hollow Nanostructured Catalyst, ACS Catal. 9 (4) (2019) 2969–2976, https://doi.org/10.1021/acscatal.9b00282.
- [39] E.N. Tseng, Y.-T. Hsiao, Y.-C. Chen, S.-Y. Chen, A. Gloter, J.-M. Song, Magnetism and plasmonic performance of mesoscopic hollow ceria spheres decorated with silver nanoparticles, Nanoscale 11 (8) (2019) 3574–3582, https://doi.org/ 10.1039/c8nr09636h.
- [40] L. Yang, M. Zhang, Y. Lan, W. Zhang, Hollow shell–corona microspheres with a mesoporous shell as potential microreactors for Au-catalyzed aerobic oxidation of alcohols, New J. Chem. 34 (7) (2010) 1355–1364, https://doi.org/10.1039/ B9N.100802K
- [41] C.M. Rochman, C. Manzano, B.T. Hentschel, S.L.M. Simonich, E. Hoh, Polystyrene Plastic: A Source and Sink for Polycyclic Aromatic Hydrocarbons in the Marine Environment, Environ. Sci. Technol. 47 (24) (2013) 13976–13984, https://doi. org/10.1021/es403605f.
- [42] L. Liu, R. Fokkink, A.A. Koelmans, Sorption of polycyclic aromatic hydrocarbons to polystyrene nanoplastic, Environ. Toxicol. Chem. 35 (7) (2016) 1650–1655, https://doi.org/10.1002/etc.3311.
- [43] N.G. Bastús, J. Comenge, V. Puntes, Kinetically Controlled Seeded Growth Synthesis of Citrate-Stabilized Gold Nanoparticles of up to 200 nm: Size Focusing versus Ostwald Ripening, Langmuir 27 (17) (2011) 11098–11105, https://doi.org/ 10.1021/la201938u.
- [44] Beer, Bestimmung der Absorption des rothen Lichts in farbigen Flüssigkeiten, Ann. Phys. 162 (5) (1852) 78–88. https://doi.org/10.1002/andp.18521620505.
- Phys. 162 (5) (1852) 78–88, https://doi.org/10.1002/andp.18521620505.
 [45] P.B. Johnson, R.W. Christy, Optical Constants of the Noble Metals, Phys. Rev. B 6 (12) (1972) 4370–4379, https://doi.org/10.1103/PhysRevB.6.4370.
- [46] J.F. Müller, K. Manomanii, M.R. Mortimer, M.S. McLachlan, Partitioning of polycyclic aromatic hydrocarbons in the polyethylene/water system, Fresenius J. Anal. Chem. 371 (6) (2001) 816–822, https://doi.org/10.1007/s002160101025.
- [47] W. Haiss, N.T.K. Thanh, J. Aveyard, D.G. Fernig, Determination of Size and Concentration of Gold Nanoparticles from UV–Vis Spectra, Anal. Chem. 79 (11) (2007) 4215–4221, https://doi.org/10.1021/ac0702084.
- [48] P.K. Jain, W. Huang, M.A. El-Sayed, On the Universal Scaling Behavior of the Distance Decay of Plasmon Coupling in Metal Nanoparticle Pairs: A Plasmon Ruler Equation, Nano Lett. 7 (7) (2007) 2080–2088, https://doi.org/10.1021/ 10771008.
- [49] S.L. Westcott, S.J. Oldenburg, T.R. Lee, N.J. Halas, Formation and Adsorption of Clusters of Gold Nanoparticles onto Functionalized Silica Nanoparticle Surfaces, Langmuir 14 (19) (1998) 5396–5401, https://doi.org/10.1021/la980380q.
- [50] A. Musyanovych, H.-J.-P. Adler, Grafting of Amino Functional Monomer onto Initiator-Modified Polystyrene Particles, Langmuir 21 (6) (2005) 2209–2217, https://doi.org/10.1021/la047960+.
- [51] Y. Lan, M. Zhang, W. Zhang, L. Yang, Enhanced Pd-catalyzed hydrogenation of olefins within polymeric microreactors under organic/aqueous biphasic conditions, Chem. Eur. J. 15 (15) (2009) 3670–3673, https://doi.org/10.1002/ chem. 200803607
- [52] Y. Huang, Z. Chen, Y. Liu, J. Yuan, Y. Zheng, Y. Nie, X. Zou, Y. Huang, Z. Zeng, Preparation and application of diacetone-based functionalized polymeric

- microspheres, Eur. Polym. J. 196 (2023) 112297, https://doi.org/10.1016/j.
- [53] S. Wang, M. Zhang, L. Zhong, W. Zhang, A strategy to immobilize noble metal nanoparticles on silica microspheres, J. Mol. Catal. A Chem. 327 (1) (2010) 92–100, https://doi.org/10.1016/j.molcata.2010.05.018.
- [54] F. Thielbeer, K. Donaldson, M. Bradley, Zeta Potential Mediated Reaction Monitoring on Nano and Microparticles, Bioconjug. Chem. 22 (2) (2011) 144–150, https://doi.org/10.1021/bc1005015.
- [55] S. Kniajanski, R.E. Colborn, B.C. Bales, O. Riccobono, A.J. Dulgar-Tulloch, J. Stein, B.I.I. Kandapallil, Synthesis of highly loaded and well-controlled magnetic beads via emulsion polymerization, J. Appl. Polym. Sci. 129 (4) (2013) 1726–1733, https://doi.org/10.1002/app.38857.
- [56] R. La Spina, V. Spampinato, D. Gilliland, I. Ojea-Jimenez, G. Ceccone, Influence of different cleaning processes on the surface chemistry of gold nanoparticles, Biointerphases 12 (3) (2017) 031003, https://doi.org/10.1116/1.4994286.
- [57] H. Xie, S. Zhu, P. Wen, D. Zhou, Y. Yin, Y. Lan, T.-C. Lee, Y. Zhang, Q. Pu, Raspberry-Like Plasmonic Nanoaggregates with Programmable Hierarchical Structures for Reproducible SERS Detection of Wastewater Pollutants and Biomarkers, Anal. Chem. 96 (44) (2024) 17620–17630, https://doi.org/10.1021/ acs.analchem.4c03533.
- [58] M. Das, D. Gangopadhyay, R. Pelc, R. Hadravov, J. Sebestik, P. Bour, Aggregation-aided SERS: Selective detection of arsenic by surface-enhanced Raman spectroscopy facilitated by colloid cross-linking, Talanta 253 (2023) 123940, https://doi.org/10.1016/j.talanta.2022.123940.
- [59] C.-Y. Liu, H.-W. Cheng, M.-Y. Lai, H.-M. Tsai, M.-Y. Liang, S. Biring, S.-W. Liu, Analyte-induced SERS hot spots for dramatically improving the ability to distinguish different concentrations of chemical solutions, J. Taiwan Inst. Chem. Eng. 165 (2024) 105769, https://doi.org/10.1016/j.jtice:2024.105769.
- [60] D. Wang, J. Zhu, B. Hui, Z. Gong, M. Fan, Halogen ion-modified silver nanoparticles for ultrasensitive surface-enhanced Raman spectroscopy detection of polycyclic aromatic hydrocarbons, Luminescence 37 (9) (2022) 1541–1546, https://doi.org/10.1002/bio.4329.

- [61] X. Gong, X. Liao, Y. Li, H. Cao, Y. Zhao, H. Li, D.P. Cassidy, Sensitive detection of polycyclic aromatic hydrocarbons with gold colloid coupled chloride ion SERS sensor, Analyst 144 (22) (2019) 6698–6705, https://doi.org/10.1039/ COANISAOL
- [62] X. Zhao, X. Luo, C.G. Bazuin, J.-F. Masson, In Situ Growth of AuNPs on Glass Nanofibers for SERS Sensors, ACS Appl. Mater. Interfaces 12 (49) (2020) 55349–55361, https://doi.org/10.1021/acsami.0c15311.
- [63] V. Montes-García, C. Fernández-López, B. Gómez, I. Pérez-Juste, L. García-Río, L. M. Liz-Marzán, J. Pérez-Juste, I. Pastoriza-Santos, Pillar[5]arene-Mediated Synthesis of Gold Nanoparticles: Size Control and Sensing Capabilities, Chemistry A European Journal 20 (27) (2014) 8404–8409, https://doi.org/10.1002/chem.201402073
- [64] M. Li, H. Yu, Y.L. Cheng, Y.H. Guo, W.R. Yao, Y.F. Xie, Simultaneous and rapid determination of polycyclic aromatic hydrocarbons by facile and green synthesis of silver nanoparticles as effective SERS substrate, Ecotoxicol. Environ. Saf. 200 (2020) 110780, https://doi.org/10.1016/j.ecoenv.2020.110780.
- [65] J. Liu, W. Cui, S. Sang, L. Guan, K. Gu, Y. Wang, J. Wang, Surface-Enhanced Raman Spectroscopic Investigation of PAHs at a Fe₃O₄@GO@Ag@PDA Composite Substrates, Micromachines 13 (8) (2022) 1253, https://doi.org/10.3390/ mii.3081.253
- [66] H.-X. Gu, K. Hu, D.-W. Li, Y.-T. Long, SERS detection of polycyclic aromatic hydrocarbons using a bare gold nanoparticles coupled film system, Analyst 141 (14) (2016) 4359–4365, https://doi.org/10.1039/C6AN00319B.
- [67] L.L. Qu, Y.T. Li, D.W. Li, J.Q. Xue, J.S. Fossey, Y.T. Long, Humic acids-based onestep fabrication of SERS substrates for detection of polycyclic aromatic hydrocarbons, Analyst 138 (5) (2013) 1523–1528, https://doi.org/10.1039/ c2an36764e.
- [68] J. Xu, J. Du, C. Jing, Y. Zhang, J. Cui, Facile Detection of Polycyclic Aromatic Hydrocarbons by a Surface-Enhanced Raman Scattering Sensor Based on the Au Coffee Ring Effect, ACS Appl. Mater. Interfaces 6 (9) (2014) 6891–6897, https://doi.org/10.1021/am500705a.